Desalination and Water Treatment
www.deswater.com
doi: 10.5004/dwt.2020.25344

188 (2020) 185–193
June

Fabrication and characterization of a visible light-driven $SrCO_3$–Ag_2CO_3 composite photocatalyst via a gas-phase co-precipitation route with CO_2

Changlin Yu[a,b,*], Mengdi Zhang[b], Qizhe Fan[a], Kai Yang[b], Wenyu Xie[a,*], Weiya Huang[b]

[a]*School of Environmental Science and Engineering, Guangdong Provincial Key Laboratory of Petrochemical Pollution Processes and Control, Guangdong University of Petrochemical Technology, Maoming, Guangdong 525000, China, emails: yuchanglinjx@163.com (C. Yu), gdmmxwy@163.com (W. Xie), 175307913@qq.com (Q. Fan)*
[b]*School of Metallurgy and Chemical Engineering, Jiangxi University of Science and Technology, 86 Hongqi Road, Ganzhou 341000, China, emails: 2391407261@qq.com (M. Zhang), 331336881@qq.com (K. Yang), 179984619@qq.com (W. Huang)*

Received 2 June 2019; Accepted 13 December 2019

ABSTRACT

Using CO_2 as the source of CO_3^{2-}, a series of novel strontium carbonate-silver carbonate ($SrCO_3$–Ag_2CO_3) composite photocatalysts with different $SrCO_3$ contents were prepared by a gas-phase co-precipitation method. The obtained $SrCO_3$–Ag_2CO_3 composites exhibited much higher photocatalytic activity than pure Ag_2CO_3 in the degradation of acid orange II under xenon lamp illumination. The obtained samples were characterized by X-ray diffraction, scanning electron microscopy, N_2 physical adsorption, UV–vis diffuse reflectance spectroscopy, X-ray photoelectron spectroscopy, Fourier transform infrared spectroscopy and photoelectrochemical measurements, respectively. With an optimal molar ratio of $SrCO_3$:Ag_2CO_3 (2:1), the composite showed the highest activity. The coupling of $SrCO_3$ into Ag_2CO_3 largely boosted the separation efficiency of photogenerated electron-hole pairs. This low-cost $SrCO_3$–Ag_2CO_3 composite photocatalysts could have promising applications in environmental purification.

Keywords: Gas-phase co-precipitation; $SrCO_3$–Ag_2CO_3 composite; Photocatalytic activity; Low cost

1. Introduction

Semiconductor photocatalytic technology shows a great potential application in solving the problems of energy shortage and environmental pollution by utilization of sunlight and it attracts great attention of researchers all over the world [1–9]. TiO_2 is the most widely studied and applied photocatalyst among various photocatalytic materials due to its high chemical stability and perfect photocatalytic activity. However, TiO_2 can only be excited by UV light which only accounts for about 3% of the whole solar energy [10–12]. Therefore, it is necessary to develop visible light-responsive photocatalytic materials.

Recently, a series of Ag-based compounds have been proved to have excellent photocatalytic activity for degradation of organic pollutants and water splitting under the illumination of visible light [5,13–20] including Ag_2O [21,22], Ag_2S [23,24], AgX (Cl, Br) [25,26], Ag_2WO_4 [27,28], Ag_3VO_4 [29,30], Ag_3PO_4 [31–33] and etc. Ag_2CO_3 is one of Ag-based semiconductors with the high visible light photocatalytic performance [34–37]. However, Ag_2CO_3 semiconductor always exhibits poor stability due to serious photo corrosion. Various strategies have been taken to overcome the limitation, for example, coupling with other semiconductors, TiO_2/Ag_2CO_3 [38], Ag_2O/Ag_2CO_3 [39–41], BiOX (Cl, Br, I)/Ag_2CO_3 [42–44], AgX/Ag_2CO_3 [45–47] and etc. [48–55]. More recently, the $CaMg(CO_3)_2$@Ag_2CO_3 microsphere photocatalyst was fabricated via a fast and low-cost ion exchange process. This $CaMg(CO_3)_2$@Ag_2CO_3 microsphere showed well-ordered hierarchical morphology with small particle sizes, which was beneficial to light absorption and the transfer of photo-generated electrons (e^-) and holes (h^+)

* Corresponding authors.

to the catalyst surface. These $CaMg(CO_3)_2$@Ag_2CO_3 microspheres showed high stability and photocatalytic activities in the degradation of acid orange II [56,57].

Normally, Ag_2CO_3 was fabricated by the precipitation method with $AgNO_3$ and Na_2CO_3 as raw materials. In this work, we attempted to use CO_2 as the carbon source to fabricate $SrCO_3$–Ag_2CO_3 composite photocatalyst via a new gas-phase co-precipitation method. To our knowledge, it is the first time to report about the fabrication of $SrCO_3$–Ag_2CO_3 composite via a gas-phase co-precipitation method.

2. Experimental setup

2.1. Catalyst synthesis

All chemicals were of analytical grade and used without further purification. The pure Ag_2CO_3 was prepared by a gas-phase precipitation method. 2 mmol $AgNO_3$ was dissolved in 20 mL deionized water and 15% $NH_3{\cdot}H_2O$ was added dropwise to the above solution until the solution became transparent. The obtained $[Ag(NH_3)_2]OH$ solution was transferred into a 50 ml Teflon-lined stainless steel autoclave and maintained the temperature at 60°C. Then the CO_2 was bubbled into $[Ag(NH_3)_2]OH$ solution and the pressure was maintained at 0.2 MPa for 3 h. After the solution was cooled down to room temperature, the precipitate was collected by filtration and washed with deionized water and absolute alcohol three times. Then, the samples were dried at 60°C for 8 h to obtain Ag_2CO_3.

To fabricate $SrCO_3$–Ag_2CO_3 composite, a certain amount of $Sr(NO_3)_2$ (0.5, 1, 2, and 3 mmol) was added into the above $[Ag(NH_3)_2]OH$ solution and stirred for 10 min. The mixture was handled in the same way to obtain the $SrCO_3$–Ag_2CO_3 with a different mole ratio of Sr^{2+}/Ag^{+}. The preparation process of the composites was shown in Fig. 1.

2.2. Catalyst characterization

The photocatalytic performance of the samples is linked to the lattice structure, specific surface area, particle morphology, optical absorption properties and bond characteristics of a photocatalyst. In order to reveal or understand the photocatalytic performance of the composites, the obtained samples were characterized by a series of physical and chemical methods. X-ray powder diffraction (XRD) was mainly used to determine the composition and crystal structure of the samples. The Bruker D8 Advance (Germany) X-ray powder diffractometer was used for analysis with a copper target (Cu Kα, λ = 0.15418 nm), where the operating voltage was 40 kV and the current was 40 mA. Scanning electron microscopy (SEM) of XL30 (Philips, Netherlands) was used to observe the apparent morphology and the particle size distribution of samples. Fourier transform infrared (FT-IR) spectra were recorded by a Nicolet-470 infrared spectrometer and the powder sample was ground to uniformity with a small amount of KBr under an infrared lamp, then molded at a pressure of 10 MPa to form a transparent sheet and scanned 16 times with a resolution of 4 cm^{-1}. The UV-vis diffuse reflectance spectra (DRS) were analyzed by Shimadzu 2550 UV-Vis-NIR spectrometer (Japan) and $BaSO_4$ was used as the standard reference. X-ray photoelectron spectroscopy (XPS) measurements were carried out on a Thermo Fisher Scientific-US ESCALAB 250Xi XPS system with a monochromatic Al Kα (hν = 1486 eV) source at a power of 150 W and a charge neutralizer. All the binding energies were referenced to the characteristic of C1s peak at 284.8 eV. The specific surface area of the sample was calculated from the N_2 adsorption-desorption curve using ASAP2020 of American Micronic Company (United States). The photocurrent analysis was carried out using the CHI660E/700E electrochemical workstation assembled by Shanghai Chenhua Instrument Co. Ltd., (China) where a Pt wire was used as the auxiliary electrode and Ag/AgCl as the reference electrode. The correlation curve between photo-generated current and time was measured with a 500 W xenon lamp used as the excitation source and a 0.1 M Na_2SO_4 solution was used as the electrolyte solution.

2.3. Photocatalytic performance measurement

The photocatalytic degradation activity of fabricated samples was carried out using a Solar-500N xenon lamp source manufactured by Beijing Newbit Technology Co. Ltd., (China) (500 W). The light intensity was 80–450 mW/cm^2. Acid Orange II (AO-II) in aqueous solution was used as the simulated pollutant. Circulating water was used to ensure the constant temperature of the pollutant solution. Firstly, a certain amount of sample (50 mg) and 20 mg/L AO-II solution (80 mL) were mixed and the suspension was stirred in the dark for 40 min to reach the adsorption and desorption equilibrium. After dark adsorption, the light source was turned on and approximately 3 mL reacted solution was sampled at regular intervals. Then, the reacted solution was centrifuged

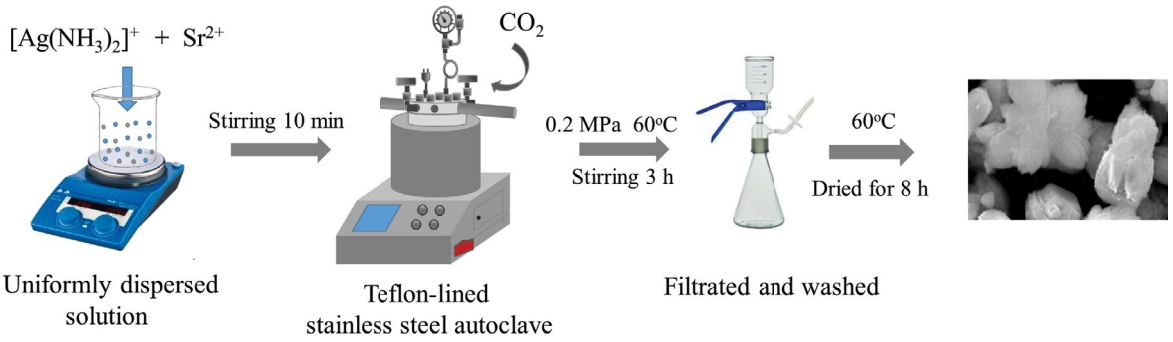

Fig. 1. Preparation diagram of $SrCO_3$-Ag_2CO_3 composites via the gas-phase co-precipitation route with CO_2.

to remove the photocatalyst powders. The concentration of AO-II was tested by a UV-vis spectrophotometer (Agilent, HP 8453, United States).

3. Results and discussion

3.1. Crystal properties

The XRD patterns of the samples are presented in Fig. 2. Sharp XRD peaks indicate their good crystallinity. It can be clearly observed that the pure Ag_2CO_3 shows distinct diffraction peaks at 18.55°, 20.54°, 32.59°, 33.67° and 39.58°, corresponding to (020), (110), (–101), (–130) and (031) crystal planes of the monoclinic phase of Ag_2CO_3 (JCPDS No.00-026-0339), respectively. Due to the formation of $SrCO_3$, new peaks at 2θ of 25.17°, 25.80°, 36.53° and 44.08° appear, which are ascribed to the orthorhombic phase of $SrCO_3$ (JCPDS No. 00-005-0418). With the increase of $SrCO_3$ content, the intensity of new peaks increases correspondingly. However, the patterns of the composites did not change greatly, which indicates that the formation of $SrCO_3$ did not change the crystal phase of Ag_2CO_3.

3.2. Specific surface area and morphological structure

The surface areas of the prepared samples were determined by N_2 physical adsorption-desorption (Fig. 3) and the results are demonstrated in Table 1. We can see that all samples show a small surface area and all most no surface area was detected for pure Ag_2CO_3. The presence of $SrCO_3$ obviously increased the surface area of the composites. From the late SEM images (Fig. 4), we can see that the morphological structure of the samples changed distinctly with the introduction of $SrCO_3$.

In Fig. 4a we see that pure Ag_2CO_3 appears cuboid particles with a length of ~6 μm, a width of ~3 μm, and a thickness of ~6 μm. The cuboid particles show a very smooth surface. The introduction of $SrCO_3$ largely changed the morphology of Ag_2CO_3. In Fig. 4b, with the 1:1 molar ratio ($SrCO_3$:Ag_2CO_3), $SrCO_3$–Ag_2CO_3 still maintains cuboid-shaped morphology, but the surface of the composite became rough. In Fig. 4c, when the molar ratio ($SrCO_3$:Ag_2CO_3) increased to 2:1, some of the composite particles transform into flower-like morphology. With a further increase in the molar ratio (3:1), Fig. 4d indicates that nearly all of the particles transform into flower-like morphology with a rough surface. Fig. 4e shows the pure $SrCO_3$ with fusiform morphology and loose surface. The increase of $SrCO_3$ resulted in a change in the texture of the composite, which is consistent with the specific surface area data of the samples in Table 1. Fig. 4f is the energy-dispersive X-ray spectroscopy (EDS) spectrum of the typical $SrCO_3$-Ag_2CO_3 (2:1) sample and it indicates the existence of Ag, Sr, C and O elements in the selected region of the composite.

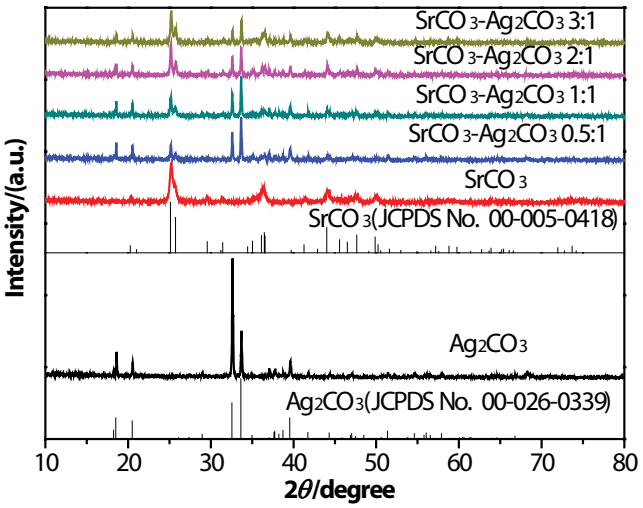

Fig. 2. XRD patterns of Ag_2CO_3, $SrCO_3$, and $SrCO_3$-Ag_2CO_3 composites.

3.3. Light absorption

The UV-Vis DRS of the samples are presented in Fig. 5a. Pure $SrCO_3$ shows no light absorption in the visible light range but obvious absorption in the UV region and pure Ag_2CO_3 exhibits excellent absorption ability in UV and visible light range. Fig. 5b indicates the band gap energies for the as-prepared catalysts calculated by the equation $(\alpha h\nu)^2 = h\nu - E_g$, where α is the absorbance, hν is the absorption energy, and E_g is the band gap energy. The band gap energies of the pure Ag_2CO_3 and pure $SrCO_3$ were estimated to be 2.55 and 3.70 eV, respectively. As for the samples of $SrCO_3$–Ag_2CO_3 with mole ratio at 1:1, 2:1 and 3:1 ($SrCO_3$:Ag_2CO_3), their band gap energies were estimated to be 2.25, 2.12, and 2.35 eV, respectively. After combining

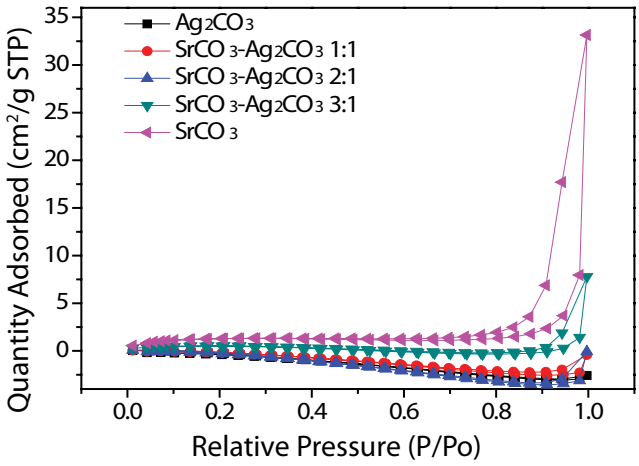

Fig. 3. Nitrogen adsorption–desorption isotherms of all samples.

Table 1
Specific surface area of the prepared samples

Sample	Specific surface area (m^2/g)
Ag_2CO_3	0
$SrCO_3$–Ag_2CO_3 (1:1)	1
$SrCO_3$–Ag_2CO_3 (2:1)	2
$SrCO_3$–Ag_2CO_3 (3:1)	3
$SrCO_3$	4

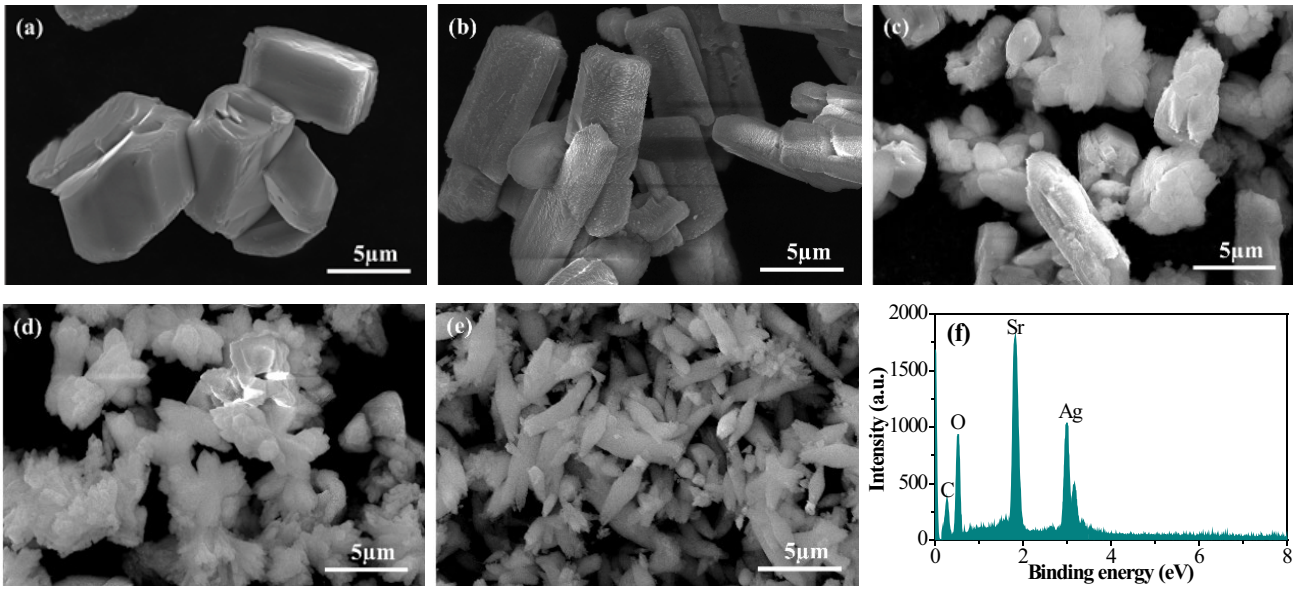

Fig. 4. SEM images of (a) Ag_2CO_3, (b) $SrCO_3$–Ag_2CO_3 (1:1), (c) $SrCO_3$–Ag_2CO_3 (2:1), (d) $SrCO_3$–Ag_2CO_3 (3:1), (e) $SrCO_3$, and (f) EDS spectrum of $SrCO_3$–Ag_2CO_3 (2:1).

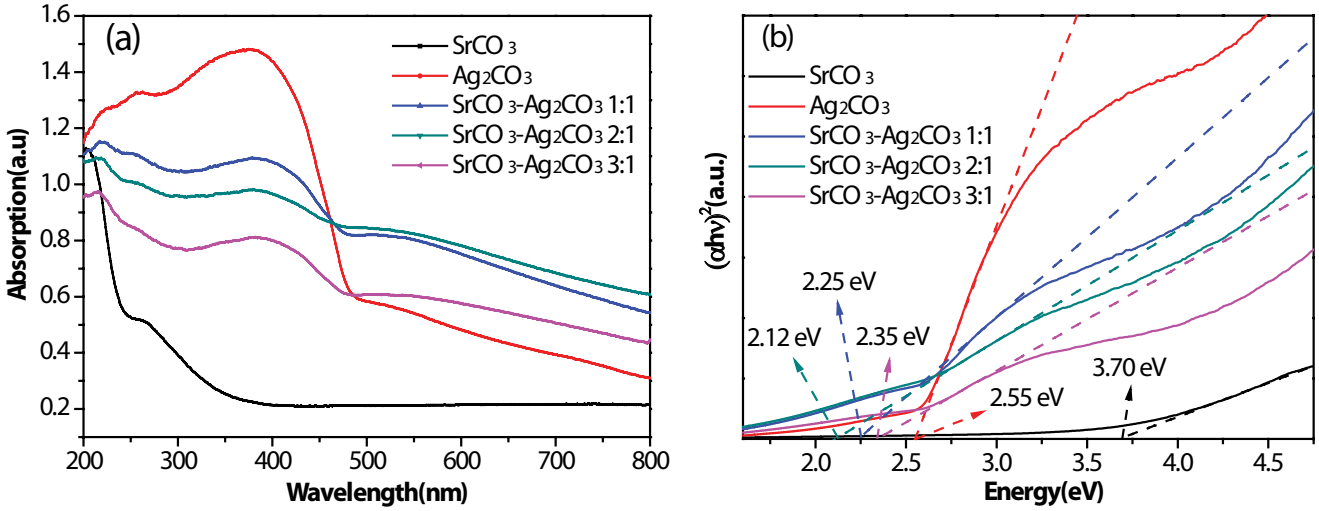

Fig. 5. Light absorption test. UV-Vis diffuse reflectance spectra of the as-prepared samples (a); Plots of $(\alpha h\nu)^2$ vs. energy ($h\nu$) for the band gap energy of samples (b).

with $SrCO_3$, the band gap energy of the composite slightly decreased compared with the pure sample, which indicates that the absorption capacity of the composite was enhanced in the visible region.

3.4. FT-IR analysis

The FT-IR spectra of the prepared samples are shown in Fig. 6. It can be clearly seen from the figure that all the composites shown a broad absorption peak near 3,430 cm^{-1}, which was considered as the characteristic stretching vibration peak of the hydroxyl group (–OH) over the surface of samples. A weak absorption peak near 1,653 cm^{-1} was ascribed to the bending vibration peak of physically adsorbed water molecules (H–O–H). Absorption peaks near 884 and 1,398 cm^{-1} were attributed to the characteristic absorption peaks of carbon anion (CO_3^{2-}) [58]. The strong and wide absorption peak of pure $SrCO_3$ near 1,474 cm^{-1} belonged to the stretching vibration peak of asymmetric C–O bond, and two absorption peaks of 857 and 702 cm^{-1} could be assigned to bending out-of-plane vibrations and in-plane vibrations, respectively. A weak and sharp absorption peak near 1,070 cm^{-1} was considered as the stretching vibration peak of symmetric C–O bond [59–61]. After the coupling of $SrCO_3$, there is no significant change in the positions of the absorption peaks corresponding to the composite samples and the intensity of the characteristic absorption peaks of CO_3^{2-} at 500–1,500 cm^{-1} gradually increased.

3.5. XPS analysis

XPS was used to characterize the valence state of elements in the $SrCO_3$–Ag_2CO_3 sample. Fig. 7 shows the high-resolution XPS spectra of $SrCO_3$–Ag_2CO_3 sample. Fig. 7a illustrates the Ag 3d spectrum and two peaks of 367.83 and 373.88 eV correspond to the Ag $3d_{3/2}$ and Ag $3d_{5/2}$, which are attributed to the existence of Ag^+ in $SrCO_3$–Ag_2CO_3. The peak of O 1s at 531.28 eV in Fig. 7b belongs to the O in Ag_2CO_3. The C 1s spectrum is displayed in Fig. 7c. The peak at 284.66 eV is ascribed to the C element in Ag_2CO_3 and the peaks located at 285.98 and 289.41 eV are associated with the C–O and C=O bands. In Fig. 7d peaks of Sr 3d at 132.68 and 134.50 eV are assigned to the Sr $3d_{3/2}$ and Sr $3d_{5/2}$, corresponding to the Sr^{2+} of $SrCO_3$ [60,61].

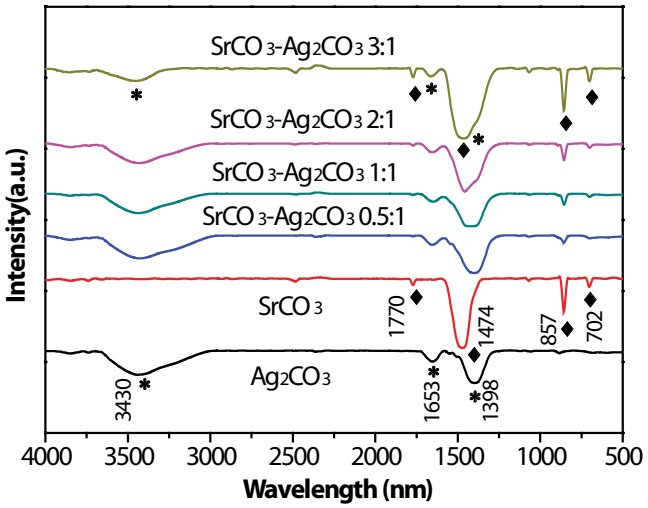

Fig. 6. FT-IR spectra of the Ag_2CO_3, $SrCO_3$ and $SrCO_3$–Ag_2CO_3 composites.

3.6. Photocurrent measurement

The transient photocurrent-time response test can be used to evaluate the migration and recombination of photo-generated electron-hole pairs. The high photocurrent intensity indicates the low recombination rate of photo-generated electrons and holes. A certain amount (15 mg) of the sample was ultrasonically dispersed and then coated on the conductive glass sheets. The result (Fig. 8) demonstrates that the photocurrent intensity was greatly improved for the composites and $SrCO_3$–Ag_2CO_3 with the mole ratio at 2:1($SrCO_3$:Ag_2CO_3) showed the largest improvement, which explained the obvious increase of photocatalytic activity. Due to the photo corrosion, the responsive intensity of photocurrent of Ag_2CO_3 decreased gradually.

3.7. Electrochemical impedance test

Electrochemical impedance spectroscopy was used to further explain the charge transfer resistance and the separation efficiency of photo-generated electron-hole pairs.

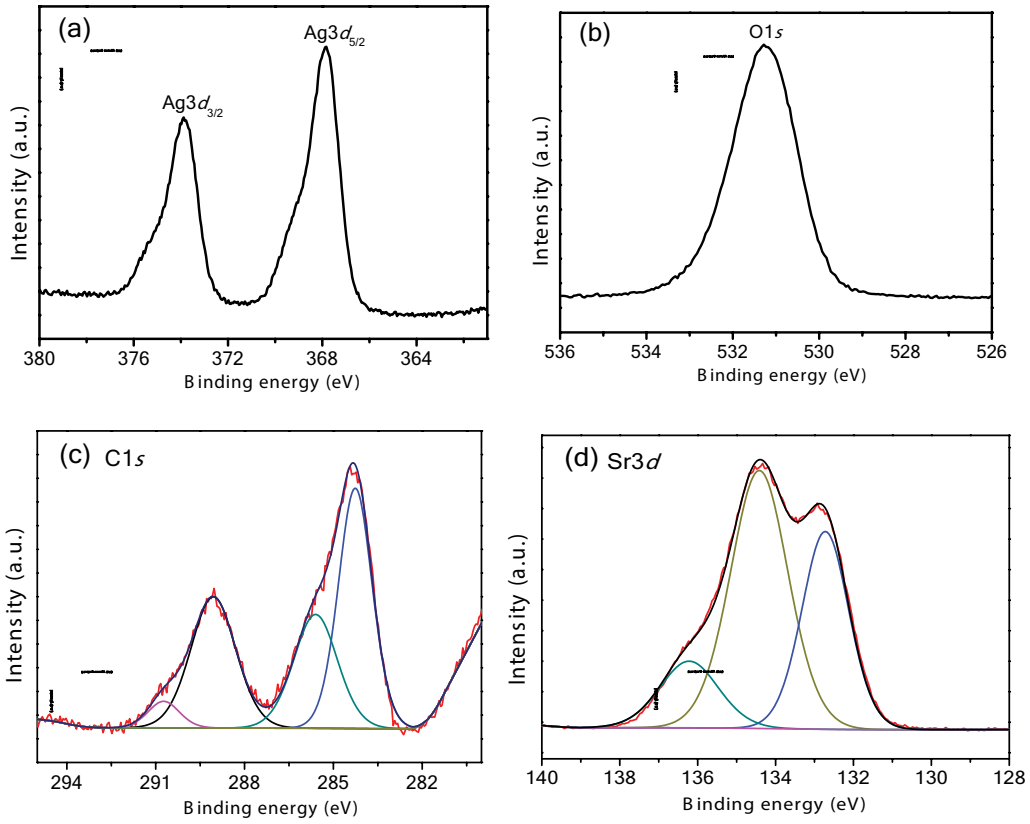

Fig. 7. High resolution XPS spectra of $SrCO_3$–Ag_2CO_3(2:1), (a) Ag 3d, (b) O 1s, (c) C 1s, and (d) Sr 3d.

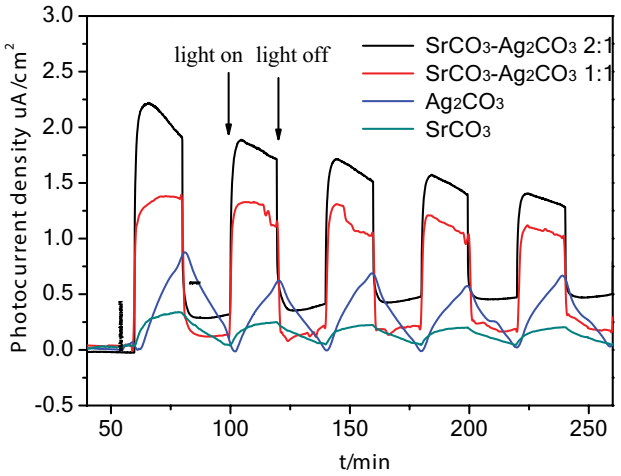

Fig. 8. Photocurrent density of the Ag_2CO_3, $SrCO_3$ and $SrCO_3$–Ag_2CO_3 samples under Xe lamp irradiation.

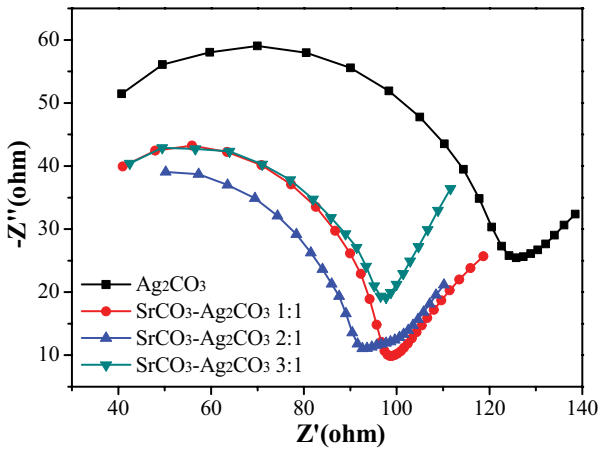

Fig. 9. Electrochemical impedance spectra of pure Ag_2CO_3, $SrCO_3$–Ag_2CO_3 (1:1), $SrCO_3$–Ag_2CO_3(2:1), and $SrCO_3$–Ag_2CO_3 (3:1).

When the working electrode was excited by charge transfer, an arc appeared on the electrochemical impedance spectrum. The smaller radius of the arc reflects the lower charge transfer resistance [62]. Fig. 9 indicates that $SrCO_3$–Ag_2CO_3 with the mole ratio at 2:1 ($SrCO_3$:Ag_2CO_3) produced the smallest arc radius. Thus, the coupling of $SrCO_3$ could result in a superior charge transfer and a high photocatalytic activity.

3.8. Photocatalytic performance

According to the concentration change of AO-II solution at different times, the degradation curve was drawn. The degradation rate was obtained by using the formula $\alpha = 1–(C/C_0)$, where C_0 is the initial concentration and C is the current concentration. In Fig. 10a we can see that pure Ag_2CO_3 shows weak photocatalytic activity and the degradation activity of the composite obviously increases with the addition of $SrCO_3$. Moreover, $SrCO_3$–Ag_2CO_3 sample with the mole ratio at 2:1($SrCO_3$:Ag_2CO_3) exhibited the maximum improvement in activity. However, with a further increase of $SrCO_3$, the activity of the composite began to decline. Fig. 10c shows the degradation rate of AO-II over different samples after visible light irradiation for 100 min and the sample of $SrCO_3$–Ag_2CO_3 with the mole ratio at 2:1 displayed the highest photocatalytic activity.

Furthermore, in order to describe the kinetics of AO-II degradation, the pseudo-first-order model was used, which is expressed by the equation $\ln(C_0/C) = kt$. The data plot of the reaction kinetics of AO-II was shown in Fig. 10b. The pseudo-first degradation rate constants of AO-II over the pure Ag_2CO_3 and the composites with the mole ratio at 0.5:1, 1:1, 2:1 and 3:1 ($SrCO_3$:Ag_2CO_3) were 0.0056, 0.0087, 0.0121, 0.0285 and 0.0140 min^{-1}, respectively.

To evaluate the stability of $SrCO_3$–Ag_2CO_3 composite, we carried out the recycling test of $SrCO_3$–Ag_2CO_3 (2:1) and Ag_2CO_3. From Fig. 11 we can see that $SrCO_3$–Ag_2CO_3 (2:1) displays the relatively higher stability than that of bare Ag_2CO_3.

In order to determine the role of the active species in the photoreaction, the photocatalytic degradation experiments of AO-II in the presence of free radical trapping agents were carried out. 1 mmol of P-benzoquinone (p-BZQ), ethylenediaminetetraacetic acid disodium (Na_2-EDTA) and tert-butyl alcohol (TBA) were added to capture oxygen negative radical ($^{\bullet}O_2^-$), photogenerated holes (h^+) and hydroxyl radical (OH), respectively. The results are shown in Fig. 9d. The degradation rate of AO-II over $SrCO_3$–Ag_2CO_3 was largely suppressed by the addition of scavengers, which indicated that·O_2^-, h^+ and·OH all participated in the degradation. The addition of Na_2-EDTA and p-BZQ leads to the greatest negative effect on degradation rate, which means that O_2^- and h^+ are the mainly primary active radicals.

The conduction band (CB) and valence band (VB) edge of semiconductor were calculated by following Eqs. (1) and (2) [63]:

$$E_{VB} = X - E_e + 0.5E_g \quad (1)$$

$$E_{CB} = E_{VB} - E_g \quad (2)$$

where X is the absolute electronegativity of the semiconductor which is defined as the geometric average of the electronegativity of the constituent atoms; E_e is the energy of free electrons on the hydrogen scale (about 4.5 eV); E_{VB} is the potential of VB edge and E_g is the band gap of the semiconductor. From the result of the UV-Vis DRS, we can see that the E_g values of $SrCO_3$ and Ag_2CO_3 are 3.70 and 2.55 eV and their X values can be calculated to 5.57 and 6.12 eV. Based on these two equations, the top of the VB and the bottom of the CB of Ag_2CO_3 were calculated as 2.70 and 0.25 eV while the VB and CB potentials of $SrCO_3$ are 2.92 and –0.78 eV.

On the basis of the above discussion, the photocatalytic mechanism of the $SrCO_3$–Ag_2CO_3 composite system is proposed in Fig. 12. Because of the difference of valence band and CB between $SrCO_3$ and Ag_2CO_3, a part of the excited electrons in the CB of Ag_2CO_3 transferred to that of $SrCO_3$. Meanwhile, the holes in the VB of $SrCO_3$ can migrate to Ag_2CO_3, which accelerated the separation efficiency of photogenerated electron-hole pairs and inhibited their

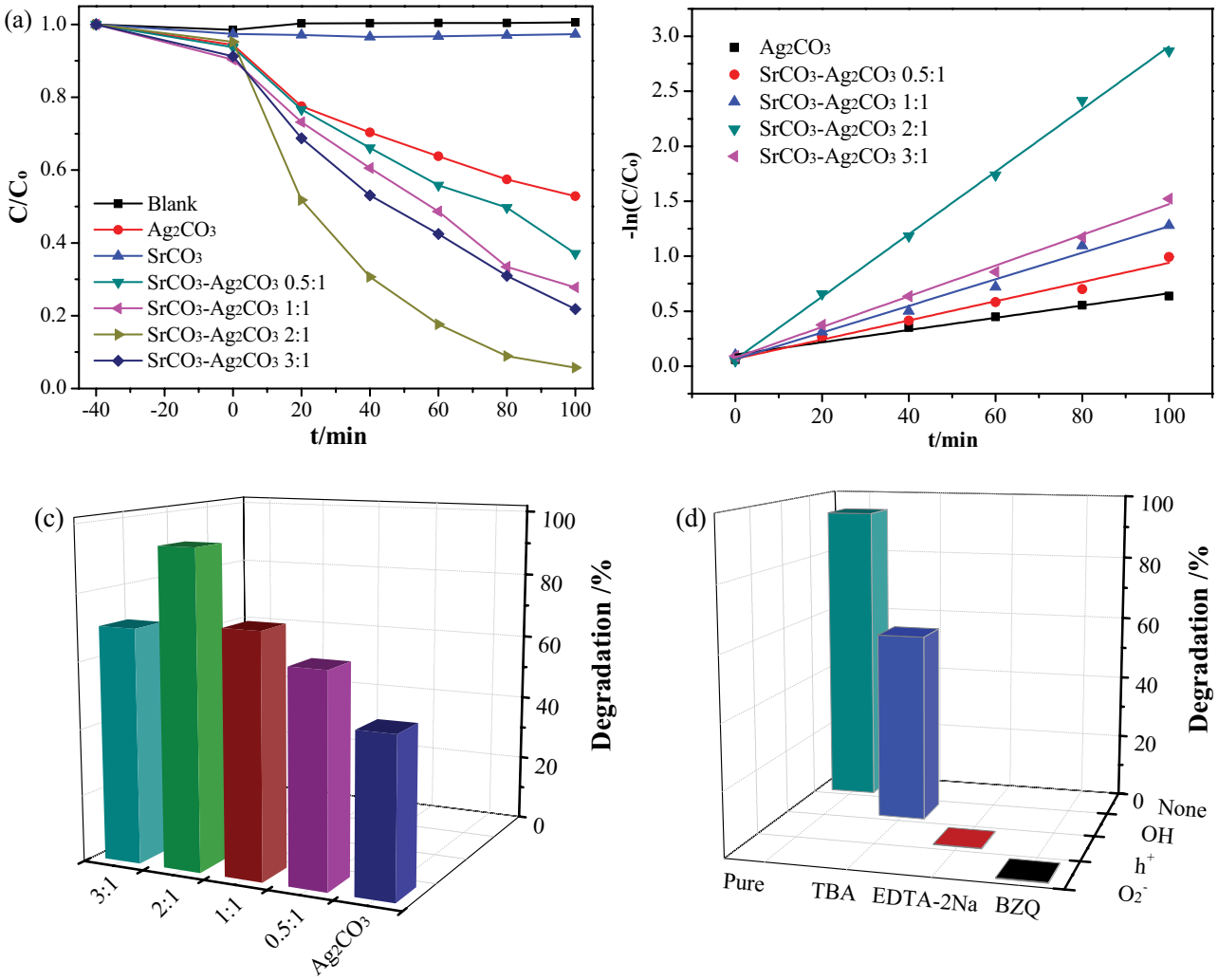

Fig. 10. Photocatalytic performance test for Ag_2CO_3, $SrCO_3$, and $SrCO_3$–Ag_2CO_3 samples, (a) Concentration change of AO-II under light irradiation, (b) reaction kinetics of acid orange II aqueous solution, (c) AO-II degradation rates over the samples and (d) effects of addition of radical-capture agents on the degradation of AO-II over $SrCO_3$–Ag_2CO_3.

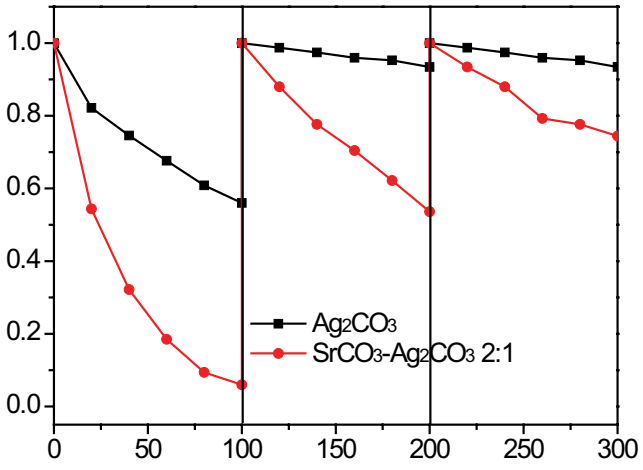

Fig. 11. Recycling test of $SrCO_3$–Ag_2CO_3 (2:1) and Ag_2CO_3 in degradation of AO-II.

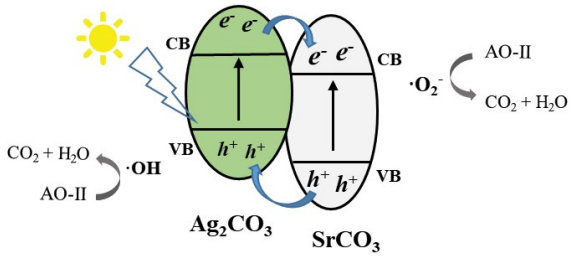

Fig. 12. Suggested photocatalytic mechanism for AO-II degradation over $SrCO_3$–Ag_2CO_3 system.

recombination. On the other hand, the presence of $SrCO_3$ increased the specific surface area, which facilitated the adsorption of the reactant molecules and broadened the absorption range of light. Therefore, more active radicals were produced for the reaction with AO-II over the surface of the photocatalysts.

4. Conclusion

In summary, a series of $SrCO_3$–Ag_2CO_3 composite photocatalysts with different $SrCO_3$ contents were successfully prepared by a gas-phase co-precipitation method. Under visible light illumination, the $SrCO_3/Ag_2CO_3$ composites exhibited high photocatalytic activity for AO-II dye degradation. The combination with $SrCO_3$ leads to a large specific surface area and strong light absorption in the visible light range. Moreover, the charge transfer resistance was reduced and the separation efficiency of photogenerated electron-hole pairs was improved, resulting in superior photocatalytic activities. This work provides with a new low-cost route to create efficient visible-light-driven Ag_2CO_3-based semiconductor photocatalysts for environmental purification.

Acknowledgements

This work was financially supported by the National Natural Science Foundation of China (No.21567008,21962006, 21707055), Guangdong Province Universities and Colleges Pearl River Scholar Funded Scheme (2019), Guangdong Basic and Applied Basic Research Foundation (2019A151501 1249), Key Research Project of Natural Science of Guangdong Provincial Department of Education (2019KZDXM010), the program for Innovative Research Team of Guangdong University of Petrochemical Technology, Academic and Technical Leaders of the Main Disciplines in Jiangxi Province (No.20172BCB22018), Jiangxi Province Natural Science Foundation (No.20181BAB213010, 20181BAB203018), Young Science Foundation of Jiangxi Province Education Office (No.GJJ160671), Open Fund of Guangdong Provincial Key Laboratory of Petrochemical Pollution Process and Control, Guangdong University of Petrochemical Technology (No. 2018B030322017).

References

[1] X.B. Chen, S.H. Shen, L.J. Guo, S.S. Mao, Semiconductor-based photocatalytic hydrogen generation, Chem. Rev., 110 (2010) 6503–6570.
[2] D.B. Zeng, K. Yang, C.L. Yu, F.Y. Chen, X.X. Li, Z. Wu, H. Liu, Phase transformation and microwave hydrothermal guided a novel double Z-scheme ternary vanadate heterojunction with highly efficient photocatalytic performance, Appl. Catal., B, 237 (2018) 449–463.
[3] C.C. Chen, W.H. Ma, J.C. Zhao, Semiconductor-mediated photodegradation of pollutants under visible-light irradiation, Chem. Soc. Rev., 39 (2010) 4206–4219.
[4] C.L. Yu, Z. Wu, R.Y. Liu, D.D. Dionysiou, K. Yang, C.Y. Wang, H. Liu, Novel fluorinated Bi_2MoO_6 nanocrystals for efficient photocatalytic removal of water organic pollutants under different light source illumination, Appl. Catal., B, 209 (2017) 1–11.
[5] R.Y. Liu, Z. Wu, J. Tian, C.L. Yu, S.Y. Li, K. Yang, X.Q. Liu, M.C. Liu, The excellent dye-photosensitized degradation performance over hierarchical BiOCl nanostructures fabricated via a facile microwave-hydrothermal process, New J. Chem., 42 (2018) 137–149.
[6] C.L. Yu, Z. Wu, R.Y. Liu, H.B. He, W.H. Fan, S.S. Xue, The effects of Gd^{3+} doping on the physical structure and photocatalytic performance of Bi_2MoO_6 nanoplate crystals, J. Phys. Chem. Solids, 93 (2016) 7–13.
[7] M.N. Chong, B. Jin, C.W.K. Chow, C. Saint, Recent developments in photocatalytic water treatment technology: a review, Water Res., 44 (2010) 2997–3027.
[8] C.L. Yu, Z. Wu, R.Y. Liu, W. Fang, Novel N/Bi-BiOCl nanoplates synthesised in NH_3 atmosphere and their enhanced photocatalytic activity, Mater. Res. Innovations, 22 (2018) 121–127.
[9] J.X. Low, J.G. Yu, M. Jaroniec, S. Wageh, A.A. Al-Ghamdi, Heterojunction photocatalysts, Adv. Mater., 29 (2017) 1601694–1601713.
[10] M. Pelaez, N.T. Nolan, S.C. Pillai, M.K. Seery, P. Falaras, A.G. Kontos, P.S.M. Dunlop, J.W.J. Hamilton, J.A. Byrne, K. O'Shea, M.H. Entezari, D.D. Dionysiou, A review on the visible light active titanium dioxide photocatalysts for environmental applications, Appl. Catal., B, 125 (2012) 331–349.
[11] J.R. Chen, F.X. Qiu, W.Z. Xu, S.S. Cao, H.J. Zhu, Recent progress in enhancing photocatalytic efficiency of TiO_2-based materials, Appl. Catal., A, 495 (2015) 131–140.
[12] M.Z. Ge, C.Y. Cao, J.Y. Huang, S.H. Li, A review of one-dimensional TiO_2 nanostructured materials for environmental and energy applications, J. Mater. Chem. A, 4 (2016) 6772–6801.
[13] H.J. Chen, L.Z. Wang, Nanostructure sensitization of transition metal oxides for visible-light photocatalysis, Beilstein J. Nanotechnol., 5 (2014) 696–710.
[14] S. Wojtyla, T. Baran, Insight on doped ZnS and its activity towards photocatalytic removing of Cr(VI) from wastewater in the presence of organic pollutants, Mater. Chem. Phys., 212 (2018) 103–112.
[15] H.J. Yu, R. Shi, Y.X. Zhao, T. Bian, Y.F. Zhao, C. Zhao, G.I.N. Waterhouse, L.Z. Wu, C.H. Tung, T.R. Zhang, Alkali-assisted synthesis of nitrogen deficient graphitic carbon nitride with tunable band structures for efficient visible-light-driven hydrogen evolution, Adv. Mater., 29 (2017) 1605148–1605154.
[16] J.D. Li, C.L. Yu, W. Fang, L.H. Zhu, W.Q. Zhou, Q.Z. Fan, Preparation, characterization and photocatalytic performance of heterostructured $AgCl/Bi_2WO_6$ microspheres, Chin. J. Catal., 36 (2015) 987–993.
[17] G.Z. Wang, H.K. Yuan, J.L. Chang, B. Wang, A.L. Kuang, H. Chen, ZnO/MoX_2 (X = S, Se) composites used for visible light photocatalysis, RSC Adv., 8 (2018) 10828–10835.
[18] H. Li, J. Li, Z.H. Ai, F.L. Jia, Oxygen vacancy-mediated photocatalysis of BiOCl: reactivity, selectivity, and perspectives, Angew. Chem. Int. Ed., 57 (2018) 122–138.
[19] Z. Wu, D.B. Zeng, X.Q. Liu, C.L. Yu, K. Yang, M.C. Liu, Hierarchical δ-$Bi_2O_3/Bi_2O_2CO_3$ composite microspheres: phase transformation fabrication, characterization and high photocatalytic performance, Res. Chem. Intermed., 44 (2018) 5995–6010.
[20] P.Y. Xiao, J.F. Lou, H.X. Zhang, W.L. Song, X.L. Wu, H.J. Lin, J. Chen, S.J. Liu, X.K. Wang, Enhanced visible-light-driven photocatalysis from WS_2 quantum dots coupled to BiOCl nanosheets: synergistic effect and mechanism insight, Catal. Sci. Technol., 8 (2018) 201–209.
[21] W. Jiang, H.Y. Fu, Y.M. Zhu, H.R. Yue, S.J. Yuan, B. Liang, Floatable superhydrophobic Ag_2O photocatalyst without a modifier and its controllable wettability by particle size adjustment, Nanoscale, 10 (2018) 13661–13672.
[22] X.J. Wen, C.G. Niu, L. Zhang, C. Liang, G.M. Zeng, A novel Ag_2O/CeO_2 heterojunction photocatalysts for photocatalytic degradation of enrofloxacin: possible degradation pathways, mineralization activity and an in depth mechanism insight, Appl. Catal., B, 221 (2018) 701–714.
[23] C.L. Yu, L.F. Wei, W.Q. Zhou, D.D. Dionysiou, L.H. Zhu, Q. Shu, H. Liu, A visible-light-driven core-shell like Ag_2S@ Ag_2CO_3 composite photocatalyst with high performance in pollutants degradation, Chemosphere, 157 (2016) 250–261.
[24] J. Tian, T.J. Yan, Z. Qiao, L.L. Wang, W.J. Li, J.M. You, B.B. Huang, Anion-exchange synthesis of Ag_2S/Ag_3PO_4 core/shell composites with enhanced visible and NIR light photocatalytic performance and the photocatalytic mechanisms, Appl. Catal., B, 209 (2017) 566–578.
[25] H. Xu, J. Yan, Y.G. Xu, Y.H. Song, H.M. Li, J.X. Xia, C.J. Huang, H.L. Wan, Novel visible-light-driven AgX/graphite-like C_3N_4 (X=Br, I) hybrid materials with synergistic photocatalytic activity, Appl. Catal., B, 129 (2013) 182–193.
[26] C. Zeng, Y.M. Hu, Y.X. Guo, T.R. Zhang, F. Dong, Y.H. Zhang, H.W. Huang, Facile in situ self-sacrifice approach to ternary hierarchical architecture Ag/AgX (X=Cl, Br, I)/

$AgIO_3$ distinctively promoting visible-light photocatalysis with composition-dependent mechanism, ACS Sustainable Chem. Eng., 4 (2016) 3305–3315.
[27] H.B. He, S.S. Xue, Z. Wu, C.L. Yu, K. Yang, L.H. Zhu, W.Q. Zhou, R.Y. Liu, Synthesis and characterization of robust Ag_2S/Ag_2WO_4 composite microrods with enhanced photocatalytic performance, J. Mater. Res., 31 (2016) 2598–2607.
[28] S. Rajamohan, V. Kumaravel, R. Muthuramalingam, S. Ayyadurai, A. Abdel-Wahab, B.S. Kwak, M. Kang, S. Sreekantan, Fe_3O_4-Ag_2WO_4: facile synthesis, characterization and visible light assisted photocatalytic activity, New J. Chem., 41 (2017) 11722–11730.
[29] S.M. Wang, D.L. Li, C. Sun, S.G. Yang, Y. Guan, H. He, Synthesis and characterization of g-C_3N_4/Ag_3VO_4 composites with significantly enhanced visible-light photocatalytic activity for triphenylmethane dye degradation, Appl. Catal., B, 144 (2014) 885–892.
[30] V.R. Raja, D.R. Rosaline, A. Suganthi, M. Rajarajan, Ultrasonic assisted synthesis with enhanced visible-light photocatalytic activity of NiO/Ag_3VO_4 nanocomposite and its antibacterial activity, Ultrason. Sonochem., 44 (2018) 73–85.
[31] C.X. Zheng, H. Yang, Z.M. Cui, H.M. Zhang, X.X. Wang, A novel $Bi_4Ti_3O_{12}$/Ag_3PO_4 heterojunction photocatalyst with enhanced photocatalytic performance, Nanoscale Res. Lett., 12 (2017) 608.
[32] H.L. Lin, H.F. Ye, B.Y. Xu, J. Cao, S.F. Chen, Ag_3PO_4 quantum dot sensitized $BiPO_4$: a novel p-n junction Ag_3PO_4/$BiPO_4$ with enhanced visible-light photocatalytic activity, Catal. Commun., 37 (2013) 55–59.
[33] J.H. Guo, H.X. Shi, X.B. Huang, H.F. Shi, Z.F. An, AgCl/Ag_3PO_4: a stable Ag-Based nanocomposite photocatalyst with enhanced photocatalytic activity for the degradation of parabens, J. Colloid Interface Sci., 515 (2018) 10–17.
[34] S.H. Guo, J.X. Bao, T. Hu, L.B. Zhang, L. Yang, J.H. Peng, C.Y. Jiang, Controllable synthesis porous Ag_2CO_3 nanorods for efficient photocatalysis, Nanoscale Res. Lett., 10 (2015) 193–200.
[35] P. Xiao, H.Y. Yuan, J.Q. Liu, Y.Y. Zheng, X.H. Bi, J.P. Zhang, Radical mechanism of isocyanide-alkyne cycloaddition by multicatalysis of Ag_2CO_3, solvent, and substrate, ACS Catal., 5 (2015) 6177–6184.
[36] C.W. Xu, Y.Y. Liu, B.B. Huang, H. Li, X.Y. Qin, X.Y. Zhang, Y. Dai, Preparation, characterization, and photocatalytic properties of silver carbonate, Appl. Surf. Sci., 257 (2011) 8732–8736.
[37] L. Zhou, L.Y. Liang, D. Talifu, A. Abuliai, Sonochemical fabrication of Ag_2CO_3 nanomaterial and influencing factors on photocatalytic properties, IOP Conf. Ser.: Mater. Sci. Eng., 167 (2017) 012032.
[38] C.L. Yu, L.F. Wei, J.C. Chen, Y. Xie, W.Q. Zhou, Q.Z. Fan, Enhancing the photocatalytic performance of commercial TiO_2 crystals by coupling with trace narrow-band-gap Ag_2CO_3, Ind. Eng. Chem. Res., 53 (2014) 5759–5766.
[39] H.Q. Wang, J.Z. Li, P.W. Huo, Y.S. Yan, Q.F. Guang, Preparation of Ag_2O/Ag_2CO_3/MWNTs composite photocatalysts for enhancement of ciprofloxacin degradation, Appl. Surf. Sci., 366 (2016) 1–8.
[40] C.L. Yu, G. Li, S. Kumar,K. Yang, R.C. Jin, Phase transformation synthesis of novel Ag_2O/Ag_2CO_3 heterostructures with high visible light efficiency in photocatalytic degradation of pollutants, Adv. Mater., 26 (2014) 892–898.
[41] X.L. Zhao, Y.C. Su, X.D. Qi, X.J. Han, A facile method to prepare novel Ag_2O/Ag_2CO_3 three-dimensional hollow hierarchical structures and their water purification function, ACS Sustainable Chem. Eng., 5 (2017) 6148–6158.
[42] S.S. Fang, C.Y. Ding, Q. Liang, Z.Y. Li, S. Xu, Y.Y. Peng, D.Y. Lu, In-situ precipitation synthesis of novel BiOCl/Ag_2CO_3, hybrids with highly efficient visible-light-driven photocatalytic activity, J. Alloys Compd., 684 (2016) 230–236.
[43] J. Wang, C. Dong, B.B. Jiang, K.L. Wu, J. Sun, X.Z. Li, W.J. Zhang, B. Zhang, X.W. Wei, Preparation of visible light-driven Ag_2CO_3/BiOBr composite photocatalysts with universal degradation abilities, Mater. Lett., 131 (2014) 108–111.
[44] N. Wang, L. Shi, L.Z. Yao, C.Y. Lu, Y. Shi, J.M. Sun, Highly improved visible-light-induced photocatalytic performance over BiOI/Ag_2CO_3 heterojunctions, RSC Adv., 8 (2018) 537–546.
[45] H. Xu, J.X. Zhu, Y.X. Song, T.T. Zhu, W.K. Zhao, Y.H. Song, Z.L. Da, C.B. Liu, H.M. Li, Fabrication of AgX-loaded Ag_2CO_3 (X=Cl, I) composites and their efficient visible-light-driven photocatalytic activity, J. Alloys Compd., 622 (2015) 347–357.
[46] H.J. Dong, G. Chen, J.X. Sun, Y.J. Feng, C.M. Li, G.H. Xiong, C.D. Lv, Highly-effective photocatalytic properties and interfacial transfer efficiencies of charge carriers for the novel Ag_2CO_3/AgX heterojunctions achieved by surface modification, Dalton Trans., 43 (2014) 7282–7289.
[47] J.J. Li, W.L. Yang, J.Q. Ning, Y.J. Zhong, Y. Hu, Rapid formation of Ag_nX (X=S, Cl, PO_4, C_2O_4) nanotubes via an acid-etching anion exchange reaction, Nanoscale, 6 (2014) 5612–5615.
[48] N. Yu, R.H. Dong, J.J. Liu, K.F. Huang, B.Y. Geng, Synthesis of Ag/Ag_2CO_3 heterostructures with high length–diameter ratios for excellent photoactivity and anti-photocorrosion, RSC Adv., 6 (2014) 103938–103943.
[49] S.Q. Liu, W. Li, G.P. Dai, Q.F. Hou, Fabrication of Ag_2CO_3/$SrCO_3$ rods with highly efficient visible-light photocatalytic activity, Rare Met. Mater. Eng., 46 (2017) 312–316.
[50] G. Dai, S. Li, S. Liu, Y. Liang, H. Zhao, Improved photocatalytic activity and stability of nano-sized Ag/Ag_2CO_3 plasmonic photocatalyst by surface modification of Fe(III) nanocluster, J. Chin. Chem. Soc., 62 (2015) 944–950.
[51] J. Tian, R.Y. Liu, Z. Liu, C.L. Yu, M.C. Liu, Boosting the photocatalytic performance of Ag_2CO_3, crystals in phenol degradation via coupling with trace N-CQDs, Chin. J. Catal., 38 (2017) 1999–2008.
[52] S.Q. Liu, S. Wang, G.P. Dai, J. Lu, K. Liu, Enhanced visible-light photocatalytic activity and stability of nano-Sized Ag_2CO_3 combined with carbon nanotubes, Acta Phys. Chim. Sin., 30 (2014) 2121–2126.
[53] G.P. Dai, S.Q. Liu, Y. Liang, K. Liu, Fabrication of a nano-sized Ag_2CO_3/reduced graphene oxide photocatalyst with enhanced visible-light photocatalytic activity and stability, RSC Adv., 4 (2014) 34226–34231.
[54] J.D. Li, L.F. Wei, C.L. Yu, W. Fang, Y. Xie, W.Q. Zhou, L.H. Zhu, Preparation and characterization of graphene oxide/Ag_2CO_3 photocatalyst and its visible light photocatalytic activity, Appl. Surf. Sci., 358 (2015) 168–174.
[55] H. Xu, Y.X. Song, Y.H. Song, J.X. Zhu, T.T. Zhu, C.B. Liu, D.X. Zhao, Q. Zhang, H.M. Li, Synthesis and characterization of g-C_3N_4/Ag_2CO_3 with enhanced visible-light photocatalytic activity for the degradation of organic pollutants, RSC Adv., 4 (2014) 34539–34547.
[56] J. Tian, Z. Liu, D.B. Zeng, C.L. Yu, X.Q. Liu, K. Yang, H. Liu, The preparation and characterization of $CaMg(CO_3)_2$@Ag_2CO_3/Ag_2S/NCQD nanocomposites and their photocatalytic performance in phenol degradation, J. Nanopart. Res., 20 (2018) 182.
[57] J. Tian, Z. Wu, Z. Liu, C.L. Yu, K. Yang, L.H. Zhu, W.Y. Huang, Y. Zhou, Low-cost and efficient visible-light-driven $CaMg(CO_3)_2$ @Ag_2CO_3 microspheres fabricated via an ion exchange route, Chin. J. Catal., 38 (2017) 1899–1908.
[58] Y.X. Song, J.X. Zhu, H. Xu, C. Wang, Y.G. Xu, H.Y. Ji, K. Wang, Q. Zhang, H.M. Li, Synthesis, characterization and visible-light photocatalytic performance of Ag_2CO_3, modified by graphene-oxide, J. Alloys Compd., 592 (2014) 258–265.
[59] S.S. Wu, S.F. Yin, H.Q. Cao, Y.X. Lu, J.F. Yin, B.J. Li, Glucosan controlled biomineralization of $SrCO_3$ complex nanostructures with superhydrophobicity and adsorption properties, J. Mater. Chem., 21 (2011) 8734–8741.
[60] P. Lu, X. Hu, Y.J. Li, M. Zhang, X.P. Liu, Y.Z. He, F. Dong, M. Fu, Z. Zhang, One-step preparation of a novel $SrCO_3$/g-C_3N_4 nanocomposite and its application in selective adsorption of crystal violet, RSC Adv., 8 (2018) 6315–6325.
[61] X.F. Wu, H. Li, L.S. Sun, J.Z. Su, J.R. Zhang, W.G. Zhang, M. Zhang, G.W. Sun, L. Zhan, M. Zhang, One-step hydrothermal synthesis of visible-light-driven $In2.77S_4$/$SrCO_3$ heterojunction with efficient photocatalytic activity for degradation of methyl orange and tetracycline, Appl. Phys. A, 124 (2018) 584–592.
[62] Y.C. Rui, H. Xiong, B. Su, H.Z. Wang, Q.H. Zhang, J.L. Xu, M.B. Peter, Liquid-liquid interface assisted synthesis of SnO_2 nanorods with tunable length for enhanced performance in dye-sensitized solar cells, Electrochim. Acta, 227 (2017) 49–60.
[63] C.L. Yu, K. Yang, Q. Shu, J.C. Yu, F.F. Cao, X. Lin, X.C. Zhou, Preparation, characterization and photocatalytic performance of Mo-doped ZnO photocatalysts, Sci. China Chem., 55 (2012) 1802–1810.